Journal of Applied Electrochemistry (2020) 50:979–991
https://doi.org/10.1007/s10800-020-01450-z

RESEARCH ARTICLE

# Flexible and free-standing polyvinyl alcohol-reduced graphene oxide-$Cu_2O$/CuO thin films for electrochemical reduction of carbon dioxide

**Anjaiah Sheelam[1] · Adil Muneeb[1,2] · Biva Talukdar[3] · Rini Ravindranath[4] · Song-Jeng Huang[2] · Chun-Hong Kuo[3] · Raman Sankar[1]**

Received: 25 February 2020 / Accepted: 19 June 2020 / Published online: 30 June 2020


## Abstract

Flexible and free-standing thin films were fabricated and employed directly as working electrodes for the electrochemical reduction of $CO_2$ in 0.5 N $KHCO_3$ at 25 °C, in which, various sizes of $Cu_2O$ nanocubes (~ 27 ± 2, 37 ± 3, 62 ± 4 and 207 ± 3 nm) with different extent of surface oxidation (13, 20, 66, and 64% of Cu(II)) were reinforced on to polyvinyl alcohol/reduced graphene oxide matrix (PVA/rGO/($Cu_2O$/CuO_X, where, X = without halide, Cl, Br and I). The size of $Cu_2O$ nanocubes and their surface oxidation were systematically altered by the addition of 1 mL of 10 mM sodium halides (NaCl, NaBr, and NaI) during the synthesis. Energy-dispersive X-ray spectroscopy mapping displayed the specific adsorption of $Cl^-$ ions over the $Cu_2O$ surface, whereas $Br^-$ and $I^-$ ions did not show such behaviour. PVA/rGO/($Cu_2O$/CuO_Cl) thin film exhibited a low overpotential of 20 mV for $CO_2$ reduction reaction and, ~ 60 and ~ 7 times higher current density at − 0.80 V vs. RHE compared to that of the PVA/rGO/($Cu_2O$/CuO), PVA/rGO/($Cu_2O$/CuO_Br) ≈ PVA/rGO/($Cu_2O$/CuO_I), respectively. Gas chromatography and $^1$H-NMR analyses confirmed methanol as the single liquid product, with a faradaic efficiency of 63% at − 0.75 V vs. RHE on PVA/rGO/($Cu_2O$/CuO_Cl) thin film.

**Graphic abstrat**

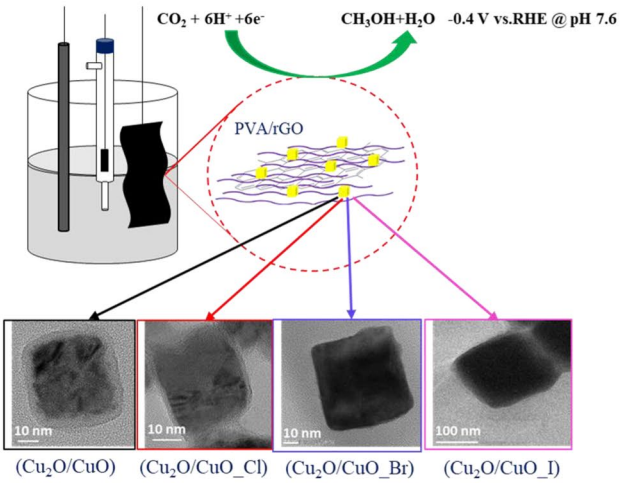


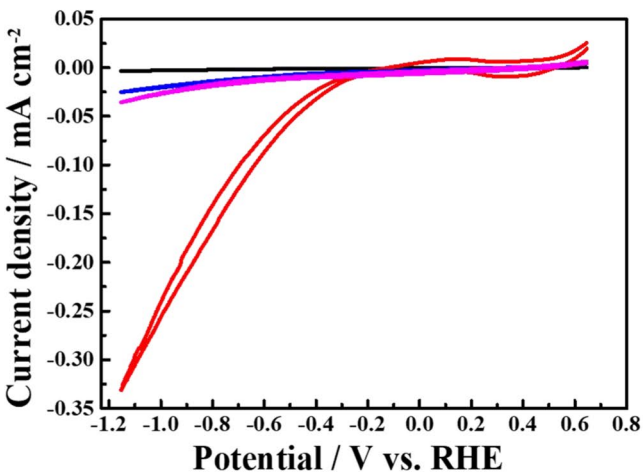


**Keywords** $CO_2$ electrochemical reduction · $^1$H-NMR · Nanocubes · Reduced graphene oxide · Thin film electrodes

**Electronic supplementary material** The online version of this article (https://doi.org/10.1007/s10800-020-01450-z) contains supplementary material, which is available to authorized users.

Extended author information available on the last page of the article

## 1 Introduction

Proliferation of carbon dioxide ($CO_2$) is identified as a major reason accountable for the disruption of our eco-system [1] Therefore, it is necessary to control $CO_2$ emissions into the atmosphere and reduce it through environment-friendly approaches. The conversion of $CO_2$ directly into industrial commodities offers double advantage which is carbon–neutral energy-dense fuel production and mitigation of $CO_2$ levels into the atmosphere [2]. Methanol is one such important industrial commodity [3, 4]. Even though there are several catalysts proposed to convert $CO_2$ to methanol, separation of methanol from several products generated is usually a time consuming, inefficient and non-scalable process [5].

For the large scale production of methanol from $CO_2$, an inexpensive, earth-abundant catalyst with facile and sustainable synthesis procedure, selectivity, and stability are extremely desirable. At commercial levels, methanol is being produced via the hydrogenation process (using syngas, i.e. CO and $H_2$) [6, 7]. However, this process requires a large amount of hydrogen, and high temperatures and pressures. $CO_2$ reduction reaction ($CO_2$RR) using electrocatalysts is an attractive green route to generate beneficial fuels such as hydrogen, methane, and methanol at room temperature and pressure [8]. Several metallic electrodes have been used as the electrocatalysts for $CO_2$RR [9–11]. Among all, Cu is an earth-abundant and relatively inexpensive element whose surface exhibits low affinity towards CO impurities/intermediates in the course of $CO_2$RR [12]. Primarily, pure Cu particles have been identified as prominent electrocatalysts for the formation of methane, ethylene, and ethanol [13]. Cuprous oxide ($Cu_2O$) is a p-type semiconductor material that has captivated several interests due to its potential applications in catalysis, gas sensing, and solar energy conversion [14]. Cu(I) species in $Cu_2O$ could directly reduce the $CO_2$ to methanol due to the facile adsorption of $CO_2$ [15]. To tune the selectivity and catalytic properties of $Cu_2O$ various shapes such as nanocubes, nanospheres, nanocages, and hollow structures with different sizes have been synthesized and employed for numerous applications in electrocatalysis [16–18].

Composite of $Cu_2O$ with conductive materials (such as carbon nanotubes, carbon cloth, rGO, graphene, and polypyrrole) is a promising strategy to improve its electrical conductivity, electrocatalytic activity, and selectivity. Multiwalled carbon nanotubes (MWCNTs) impregnated $Cu_2O$ was evaluated for $CO_2$ reduction to methanol, in which MWCNTs stabilizes Cu(I) at the defects of MWCNTs and prevents the formation of Cu(II) [19]. Lower current densities were observed at higher loadings (40–50 wt. %) of $Cu_2O$ on MWCNTs due to the agglomeration of $Cu_2O$, which eventually reduces the effective surface area and active sites. Tang and co-workers reported enhanced stability of $Cu_2O$/rGO composite due to the efficient charge transfer from $Cu_2O$ to rGO. They also observed an improved photoelectrocatalytic reduction of $CO_2$ to CO on $Cu_2O$/rGO composite [20]. $Cu_2O$ supported gas diffusion electrodes have been investigated for the electrochemical reduction of $CO_2$ in 0.5 M $KHCO_3$ [21]. These electrodes have produced mainly methanol (faradaic efficiency, FE, 42.3%), small quantities of ethanol (FE = 10.1%) and n-propanol (FE = 2.4%), whereas, graphene-supported $Cu_2O$ electrode has produced exclusively ethanol with FE of 9.93%. Wu and co-workers studied the electrochemical reduction of $CO_2$ on $Cu_2O$ cubes (640 nm) deposited carbon clothes (E-TEK) in 0.5 M NaOH electrolyte [22]. Gas chromatography confirmed methanol as the predominant product on $Cu_2O$ cubes deposited carbon cloth. Recently, Chang and co-workers prepared the octahedral shaped $Cu_2O$ with low index facets and icosahedra shaped $Cu_2O$ particles with high index facets followed by functionalization with polypyrrole on a flexible linen paper ($Cu_2O_{(OL\text{-}MH)}$/ppy coated LT paper) for the selective formation of methanol (FE = 93%) from $CO_2$RR [23].

Salazar-Villapando and co-workers observed the enhanced current densities during the $CO_2$RR by adding KCl, KBr and KI salts into the aqueous electrolytes [24]. Even though they haven't analyzed the products of $CO_2$RR, the enhanced current densities are ascribed due to facile electron transfer from Cu-halides to the vacant orbital of $CO_2$. Strasser and Co-workers demonstrated the effect of adding the halides ($Cl^-$, $Br^-$ and $I^-$) to the electrolyte on the electrocatalytic activity and selectivity of Cu electrode in $CO_2$RR [25]. The presence of $Cl^-$ and $Br^-$ aided the increased selectivity of CO formation, while the $I^-$ increased the methane production. The effect was ascertained to the high transfer of negative charge to the Cu surface, which eventually favors the protonation of CO to form methane.

Here, we propose the fabrication of scalable free-standing thin films as working electrodes for the electrochemical reduction of $CO_2$ to methanol, in which, surface oxidized $Cu_2O$ nanocubes ($Cu_2O$/CuO, $Cu_2O$/CuO_X, where X = Cl, Br, I) were supported on polyvinyl alcohol/rGO (rGO/PVA) matrix (PVA/rGO/($Cu_2O$/CuO_X)). The fabrication of films on the inexpensive microscopic glass slide was conducted at ambient conditions. Various sizes of copper oxide nanocubes (~ 27 ± 2, 37 ± 3, 62 ± 4 and 207 ± 3 nm) and different extent of surface oxidation (CuO formation) were formed due to the addition of sodium halides (NaCl, NaBr, and NaI) during the synthesis. PVA interlocks rGO via hydrogen bonding and directs the formation of flexible thin films, while $Cu_2O$/CuO nanocubes are anchored into the matrix of PVA/rGO [26, 27]. The free-standing film, PVA/rGO/($Cu_2O$/CuO_Cl) prepared using $Cu_2O$/CuO_Cl (~ 27 nm) displays ~ 60 and ~ 7

times higher current density compared to that of the PVA/rGO/($Cu_2O$/CuO), PVA/rGO/($Cu_2O$/CuO_Br) ≈ PVA/rGO/($Cu_2O$/CuO_I) films at − 0.80 V vs. RHE, respectively. To achieve the optimum $CO_2$RR activity, the thickness of the films and loading of $Cu_2O$/CuO_Cl were studied by varying the volumes of PVA/rGO/($Cu_2O$/CuO_Cl) and $Cu_2O$/CuO_Cl solutions respectively.

## 2 Experimental section

### 2.1 Materials

Graphene oxide (GO) dispersed in water (5 g $L^{-1}$) was obtained from UniRegion Bio-Tech (Hsinchu, Taiwan). Hydrazine monohydrate (98%) and potassium hydrogen carbonate ($KHCO_3$) were purchased from Alfa Aesar (Ward Hill, MA, USA). 15 mm length and 6 mm diameter Graphite rod was purchased from Alfa Aesar, USA. Fructose (99%), PVA (average molecular weight: 10,000) and sodium chloride were obtained from Sigma-Aldrich (St. Louis, MO, USA). Ascorbic acid (≥ 99%), $Cu(NO_3)_2{\cdot}3H_2O$ (99%), sodium bromide (99.5%), and sodium iodide (99%) were purchased from Acros Organics (Geel, Belgium). Ultrapure water (18.2 MΩ cm) was obtained using a Milli-Q ultrapure system from Merck Millipore (Billerica, MA, USA). Dimethyl sulfoxide unhydrous (DMSO) (> 99.9%) and $D_2O$ (99.9 at.% D) solvents were procured from Sigma-Aldrich, USA.

### 2.2 Methods

X-ray diffraction (XRD) patterns of thin films were recorded using Bruker-8 fitted with Cu $K_\alpha$ radiation (λ = 1.54056 Å). Zeta-potential of PVA/rGO, $Cu_2O$/CuO and $Cu_2O$/CuO_X nanocubes were measured using Zetasizer Nano ZS from Malvern Panalytical, United Kingdom. Raman spectrum of GO, rGO, and PVA/rGO films were obtained using Dongwoo Optron, KyungGiDo, Korea (532 nm laser source) at an accumulation time of 5 min. Keithly 2100/220 digital multimeter, USA was used to measure the conductivity in two probe method. Hitachi S-2400 (Hitachi High-Technologies, Tokyo, Japan) scanning electron microscope (SEM) was used to measure the thickness of PVA/rGO/($Cu_2O$/CuO_Cl) films. High-resolution transmission electron microscope (HR-TEM), JSM-1200EX II was employed to measure the size of $Cu_2O$/CuO, $Cu_2O$/CuO_Cl, $Cu_2O$/CuO_Br, and $Cu_2O$/CuO_I nanocubes as well as their elemental mapping. A VG ECSA210 electron microscope from VG scientific (West Sussex, UK) was employed for X-ray photoelectron spectroscopy (XPS) measurements of various copper-based nanocubes. The electrochemical analysis was performed using a CHI 760D from CH Instruments (Austin, TX, USA). An HP 6890 series Gas Chromatography system fitted with an HP 5973 Mass Selective Detector from Agilent Technologies, Inc. (Wilmington, Delaware, USA) was used to analyze the methanol formed during $CO_2$RR. Prior to acquiring the chromatograms, the column and inlet temperatures were set at 60 and 170 °C, respectively. The gas phase ($H_2$ gas) product was detected by GC-Agilent 7890B equipped with a Restek ShinCarbon ST100/200 mesh (2.0 m in length, 1/16 inch outer diameter and 1.0 mm inner diameter) and operated at oven temperature of 40 °C with $N_2$ as carrier gas. The $H_2$ gas was detected by thermal conductivity detector (TCD). The $CO_2$RR experiment was conducted for an hour in an airtight 2 mL reaction vessel to quantify the gas and liquid products at − 0.75, − 0.80 and − 0.85 V vs. RHE. The required amount of 0.5 M $KHCO_3$ electrolyte (500 µL) was collected from the 2 mL headspace reaction vessel by gas-tight syringe and injected to GC instrument. AVIII600, Bruker Avance™ Nuclear Magnetic Resonance (NMR) spectrometer was used to detect and quantify the methanol amounts. 10 mM of DMSO was added in to the $D_2O$ solvent and used as internal standard solution for the $^1$H-NMR.

### 2.3 $Cu_2O$/CuO and $Cu_2O$/CuO_X (where X = Cl, Br, I) nanocubes synthesis

The synthesis of $Cu_2O$ nanocubes was carried out based on a previously reported work with slight modifications [28]. In addition, three different $Cu_2O$ nanocubes were synthesized using NaCl, NaBr and NaI solutions. Briefly, 2.5 mL of 0.01 M $Cu(NO_3)_2$ $3H_2O$, and 1.2 g of fructose were added into a 200 mL of double neck round bottom flask, followed by the addition of 2.5 mL of 1 M NaOH and 5 mL of 0.0788 M L-ascorbic acid. The resultant solution was diluted to 100 mL with ultrapure water. Thus prepared solution (pH 12.2) was mildly stirred for 1 h at room temperature. The resulting solution was centrifuged at a relative centrifugal force (RCF) of 20,000×*g* for 20 min and re-suspended in ultrapure water. The same centrifugation procedure was repeated about three times to remove the unreacted species. The $Cu_2O$ nanoparticle solutions were stored at − 4 °C to avoid over-oxidation of the surface. However, partial oxidation of surface is inevitable due to the atmospheric oxygen. A similar procedure was followed by the addition of 1 mL of 10 mM NaCl, NaBr, or NaI aqueous solutions after the L-ascorbic acid. Thus synthesized copper oxide nanocubes are referred to as $Cu_2O$/CuO, $Cu_2O$/CuO_Cl, $Cu_2O$/CuO_Br, and $Cu_2O$/CuO_I respectively. Each 1 mL of $Cu_2O$/CuO and $Cu_2O$/CuO_X solutions were dried at 60 °C to determine the weight of $Cu_2O$/CuO. The weight of nanocubes in 1 mL of $Cu_2O$/CuO, $Cu_2O$/CuO_Cl, $Cu_2O$/CuO_Br, and $Cu_2O$/CuO_I was found to be 45 ± 3, 42, ± 4, 30 ± 6 and 35 ± 5 µg, respectively.

### 2.4 Preparation of PVA/rGO composite

10 mL of 5 wt.% PVA aqueous solution was added to 10 mL (50 mg) of GO aqueous solution. Thus resulted PVA-GO mixture was sonicated for 30 min to achieve a homogeneous dispersion. 0.5 mL of hydrazine was added to the PVA-GO solution and heated at 95 °C for 3 h to form the PVA/rGO composite. The resulting solution was cooled and stored at ambient conditions for further use.

### 2.5 Synthesis of free-standing PVA/rGO/($Cu_2O$/CuO or $Cu_2O$/CuO_X) thin films

PVA/rGO/($Cu_2O$/CuO or $Cu_2O$/CuO_X) ink like dispersion was prepared by adding 1.31 µg of $Cu_2O$/CuO or $Cu_2O$/CuO_X solution to PVA/rGO solution containing 1 mg of rGO, followed by 1 h of sonication. Thus resulted ink was transferred to (5 × 2) $cm^2$ area of a microscopic glass mold and dried overnight for solvent evaporation at room temperature. The drying process led to the formation of a thin film, which was carefully peeled off from the glass mold and stored at − 4 °C to avoid the further oxidation of the nanocubes. $Cu_2O$/CuO_Cl loadings ($\mu g_{Cu_2O}$/CuO_Cl/$mg_{rGO}$) and free-standing film thickness ($mg_{rGO}/cm^2$) were optimized to achieve high $CO_2$RR activity. Without incorporating any physical or mechanical support and time-consuming post modifications, all electrochemical measurements were conducted directly on thin films.

### 2.6 Electrochemical measurements

Electrochemical $CO_2$RR was performed using PVA/rGO/($Cu_2O$/CuO or $Cu_2O$/CuO_X) thin films as a working electrode, Ag/AgCl (sat. KCl) electrode as a reference electrode and graphite rod as a counter electrode. The working area of the film was maintained to 1 $cm^2$. All potentials measured against the Ag/AgCl reference electrode were then converted to a reversible hydrogen electrode (RHE). The electrolyte was saturated with $CO_2$ by purging the $CO_2$ gas (30 mL/min) into the electrolyte for about 30 min. The pH of the $CO_2$-saturated 0.5 M $KHCO_3$ aqueous solution was determined to be 7.6. During the electrochemical measurements, $CO_2$ gas was continuously purged above the electrolyte. Cyclic voltammetry (CV) was performed to monitor the electrolysis of $CO_2$ using a CHI 760D electrochemical workstation, which was operated in the potential range between 0.68 and − 1.18 V vs. RHE at a scan rate of 20 mV $s^{-1}$. The amount of methanol formed was determined using a calibration plot obtained from the peak area against the concentration of standard methanol in 0.5 M $KHCO_3$ solutions.

## 3 Results and discussion

### 3.1 Formation and characterization of free-standing PVA/rGO/($Cu_2O$/CuO or $Cu_2O$/CuO_X) thin films

Successful preparation of $Cu_2O$ nanocubes was achieved only in alkaline (pH 12.2) conditions by using $Cu(NO_3)_2$ $3H_2O$, fructose and ascorbic acid. The $Cu^{2+}$ ions were stabilized by fructose via Cu(OH)-fructose complexation followed by the reduction to $Cu_2O$. However, considering the partial surface oxidation of $Cu_2O$, the nanocubes were designated as $Cu_2O$/CuO. The growth rate, size, and morphology of $Cu_2O$ can be tuned by the presence of halides in the solution, where different halides possess different adsorption strengths on the crystal facets of $Cu_2O$ [29]. The addition of 1 mL of 10 mM sodium halides (NaCl, NaBr, or NaI) during the synthesis of nanocubes alters the ionic strength of the solution, which affects the growth of Cu adatoms and hence the size of nanocubes [30, 31]. Scheme 1a illustrates the step-wise processes involved in the synthesis of $Cu_2O$/CuO nanocubes. Figure 1a–d displays HR-TEM images of $Cu_2O$/CuO, $Cu_2O$/CuO_Cl, $Cu_2O$/CuO_Br, and $Cu_2O$/CuO_I nanocubes, respectively. The average size of $Cu_2O$/CuO nanocubes was calculated to be 37 ± 3 nm, while the presence of $Cl^-$ ions led to the formation of 10 nm smaller $Cu_2O$/CuO_Cl nanocubes. While conducting the same synthesis procedure in presence of $Br^-$ or $I^-$, larger particles were formed with average diameters of 62 ± 4 and 207 ± 3 nm, respectively. Figure S1(A) shows the energy dispersive X-ray spectroscopy (EDS) mapping of Cu, $Cl^-$, $Br^-$ and $I^-$ elements. Figure S1(B) displays the EDS spectrum of the $Cu_2O$/CuO_Cl, $Cu_2O$/CuO_Br, and $Cu_2O$/CuO_I nanocubes. The EDS mapping unambiguously displays the spatial distribution of $Cl^-$ ions with at.% of 0.39 on the surface of nanocubes, confirming the specificity of $Cl^-$ ion adsorption over the surface of $Cu_2O$. Hence, the growth of $Cu_2O$ cubes was ceased by the preferable adsorption of $Cl^-$ ions over the surface of $Cu_2O$, which resulted in smaller nanocubes. The adsorbed $Cl^-$ ions thermodynamically stabilizes the surface structures and increases the surface area of $Cu_2O$/CuO_Cl [29, 32]. Random and lower intensities of purple dots were observed in Figure S1(A)b″ and c″, which indicates the presence $Br^-$ and $I^-$ ions without any specific adsorption on the surface of nanocubes. In addition, the at.% of Cl (0.39%) is higher than the $Br^-$ (0.20%) and $I^-$ (0.31%) elements. Ignaczak et al. has shown that the decrease in adsorption energy while going from $F^-$ to $I^-$ on the Cu, Ag and Au metals via density functional theory calculations [33]. XPS is a sensitive technique to gain insight into the surface composition and electronic

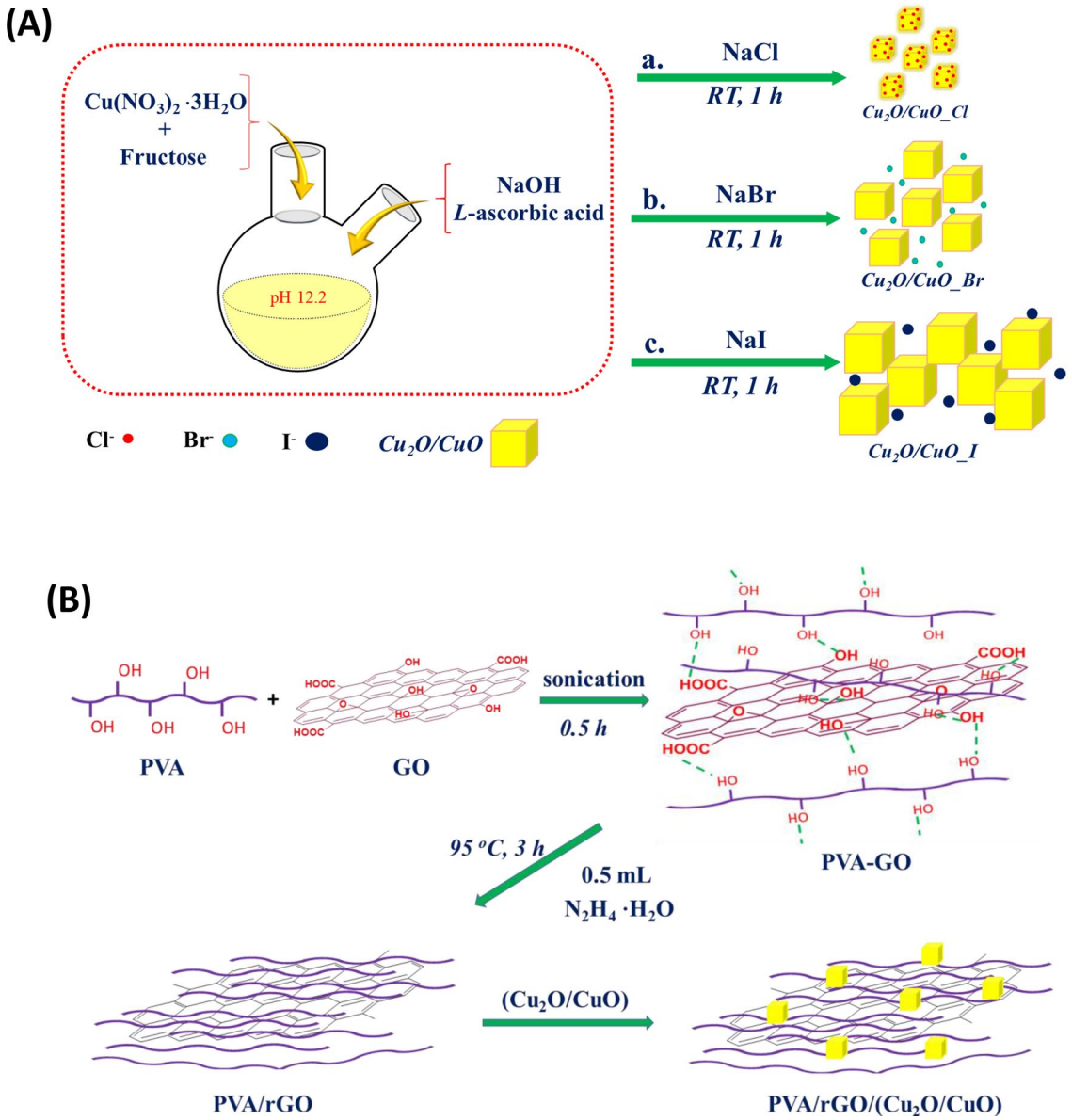


**Scheme 1** Schematic representation of (**A**) synthesis of (a) $Cu_2O$/CuO_Cl, (b) $Cu_2O$/CuO_Br, (c) $Cu_2O$/CuO_I, nanocubes, (B) preparation of PVA/rGO followed by PVA/rGO/($Cu_2O$/CuO) composite

state of the species. The surface of $Cu_2O$ could undergo oxidation in ambient conditions and leave the surface of nanocubes with mixed oxidation states of Cu (such as $Cu^+$ and $Cu^{2+}$) [34]. Quantification of the relative amount of Cu(II) species on the $Cu_2O$ surface could give an insight into the catalytic activity of $Cu_2O$ nanocubes [35]. The ratios of Cu (I): Cu(II) was calculated from the $Cu_{2p3/2}$ spectra using the methodology developed by Gerson and Jaseniak [36]. Figure 2 shows the Cu 2p core level profile XPS spectra of as-synthesized (a) $Cu_2O$/CuO, (b) $Cu_2O$/CuO_Cl, (c) $Cu_2O$/CuO_Br and (d) $Cu_2O$/CuO_I nanocubes. The deconvoluted XPS spectra of (a), (b), (c) and (d) displays the $Cu_{2p3/2}$ level at 934.3, 934.2, 933.1 and 933.0 eV; $Cu_{2p1/2}$ level at 954.3, 954.3, 954.0 and 952.8 eV respectively, which can be assigned to $Cu^+$ present in $Cu_2O$. Particularly, $Cu_2O$/CuO_Cl, $Cu_2O$/CuO_Br, and $Cu_2O$/CuO_I nanocubes show peaks at 936.9, 935.0 and 934.9 eV respectively, these peaks can be assigned to $Cu^{2+}$, which indicates the formation of CuO surface layer. The main peak present (935.0 and 934.9 eV) in $Cu_2O$/CuO_Br and $Cu_2O$/CuO_I nanocubes indicates the significant oxide layer over the $Cu_2O$ surface. Hence, the availability of $Cu_2O$ active sites to the $CO_2$RR has diminished significantly. $Cu_2O$/CuO_Cl nanocubes consist of mainly $Cu_2O$ species (80%) with a minor surface CuO phase (20%). Peaks at 944.1, 944.5, 941.0, 942.0; 949.9 eV were

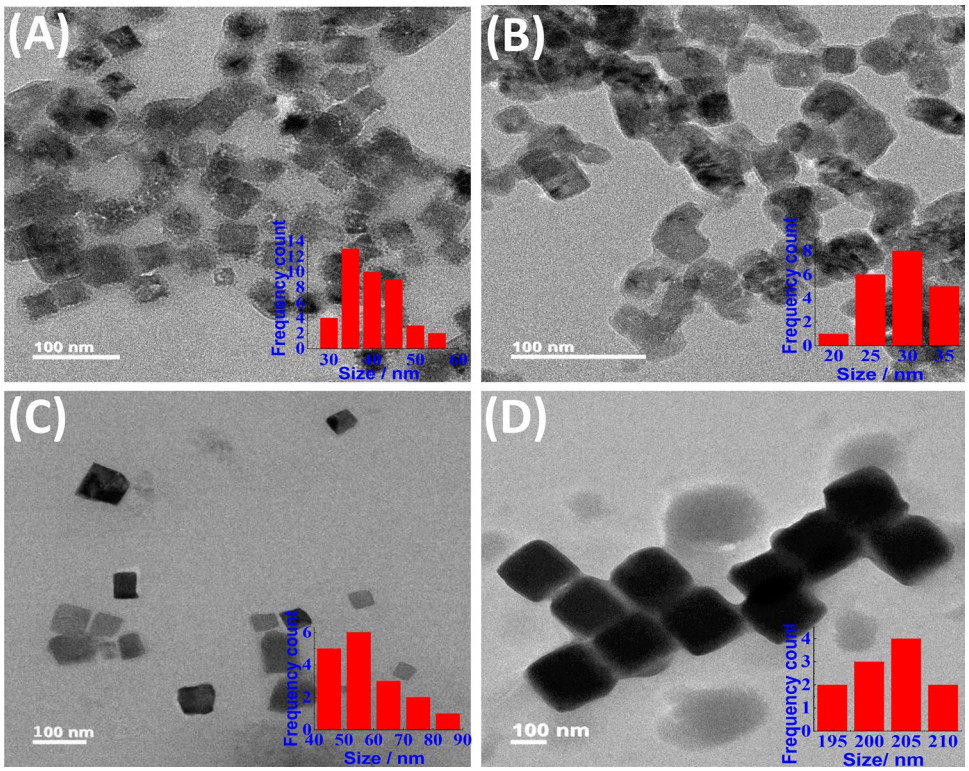


**Fig. 1** HR-TEM images, **a** $Cu_2O/CuO$, **b** $Cu_2O/CuO\_Cl$, **c** $Cu_2O/CuO\_Br$ and **d** $Cu_2O/CuO\_I$ nanocubes, inset graphs represents the size distribution of corresponding nanocubes, respectively.

identified as the satellite peaks of CuO $Cu_{2p3/2}$ and 963.8, 963.9, 963.5 and 963.5 eV were identified as the satellite peaks of CuO $Cu_{2p1/2}$ level. The ratios of $Cu_2O$: CuO for (a) $Cu_2O/CuO$, (b) $Cu_2O/CuO\_Cl$, (c) $Cu_2O/CuO\_Br$ and (d) $Cu_2O/CuO\_I$ was calculated to be 87:13, 80:20, 34:66 and 35:65.

PVA is a polymer containing hydroxyl functional groups with excellent chemical stability and film-forming ability [37]. Scheme 1b shows the synthesis of PVA/rGO and PVA/rGO/($Cu_2O$/CuO) composites. An equal volume ratio of 5 wt.% PVA and GO aqueous solutions were thoroughly mixed to obtain a PVA-GO solution. The hydroxyl groups in PVA interact with each other via intra-molecular hydrogen bonding. GO could interact with the hydroxyl groups of PVA via intermolecular hydrogen bonding, which is then reduced by hydrazine at 90 °C for 3 h to form a macroscopically homogeneous PVA/rGO solution [26]. The brown color of the PVA-GO solution, slowly converted to black, indicating the formation of rGO. Raman spectroscopy was employed to confirm the formation of rGO from GO. Figure 3a shows the comparison of Raman spectra of GO, rGO, and PVA/rGO composites. D- and G-band of all the three samples were observed at 1346 and 1582 $cm^{-1}$, respectively. The D- and G-bands originated from the first-order scattering of $E_{2g}$ vibrational modes in the graphitic forms ($sp^2$-carbon) and defects ($sp^3$-carbon), respectively. In the Raman spectrum of rGO and PVA/rGO, D-band intensity decreased while G-band becomes prominent. D-band to G-band ratio (D/G ratio) for GO, rGO and PVA/rGO is found to be 1.451, 0.851 and 0.671, respectively. The decrease in the D/G ratio of PVA/rGO composite confirms the formation of rGO and $sp^2$ networks on the basal planes through the hydrazine reduction [38].

The electrostatic interactions between the $Cu_2O$ and PVA/rGO are one of the possible forces governing the affinity of nanocubes into the network rGO/PVA matrix. Hence, ζ-potential measurements were conducted to assess the electrostatic interactions between PVA/rGO and $Cu_2O$/CuO or $Cu_2O/CuO\_X$ nanocubes. Table 1 shows the ζ-potential values for the aqueous solutions of PVA/rGO, $Cu_2O/CuO$, $Cu_2O/CuO\_Cl$, $Cu_2O/CuO\_Br$, and $Cu_2O/CuO\_I$ nanocubes along with their corresponding standard deviation. The ζ-potential of PVA/rGO was found to be − 6.34 mV with a standard deviation of ± 0.14 mV. The negative ζ-potential value indicates the presence of anionic sites over the PVA/rGO matrix for the adsorption of cationic species. However, ζ-potential values for $Cu_2O$/CuO, $Cu_2O/CuO\_Cl$, $Cu_2O/CuO\_Br$, and $Cu_2O/CuO\_I$ nanocubes were also observed to be negative which were − 19.16, − 13.50, − 38.43 and − 36.26 mV, respectively. The nanocubes which posses the high negative ζ-potential will be repelled stronger from PVA/rGO matrix and hence, weaker attractive forces are expected. The weak electrostatic attractions would operate between PVA/rGO and $Cu_2O/CuO$, $Cu_2O/CuO\_Br$, and $Cu_2O/CuO\_I$ compared to that of the PVA/rGO and $Cu_2O/CuO\_Cl$ nanocubes. The

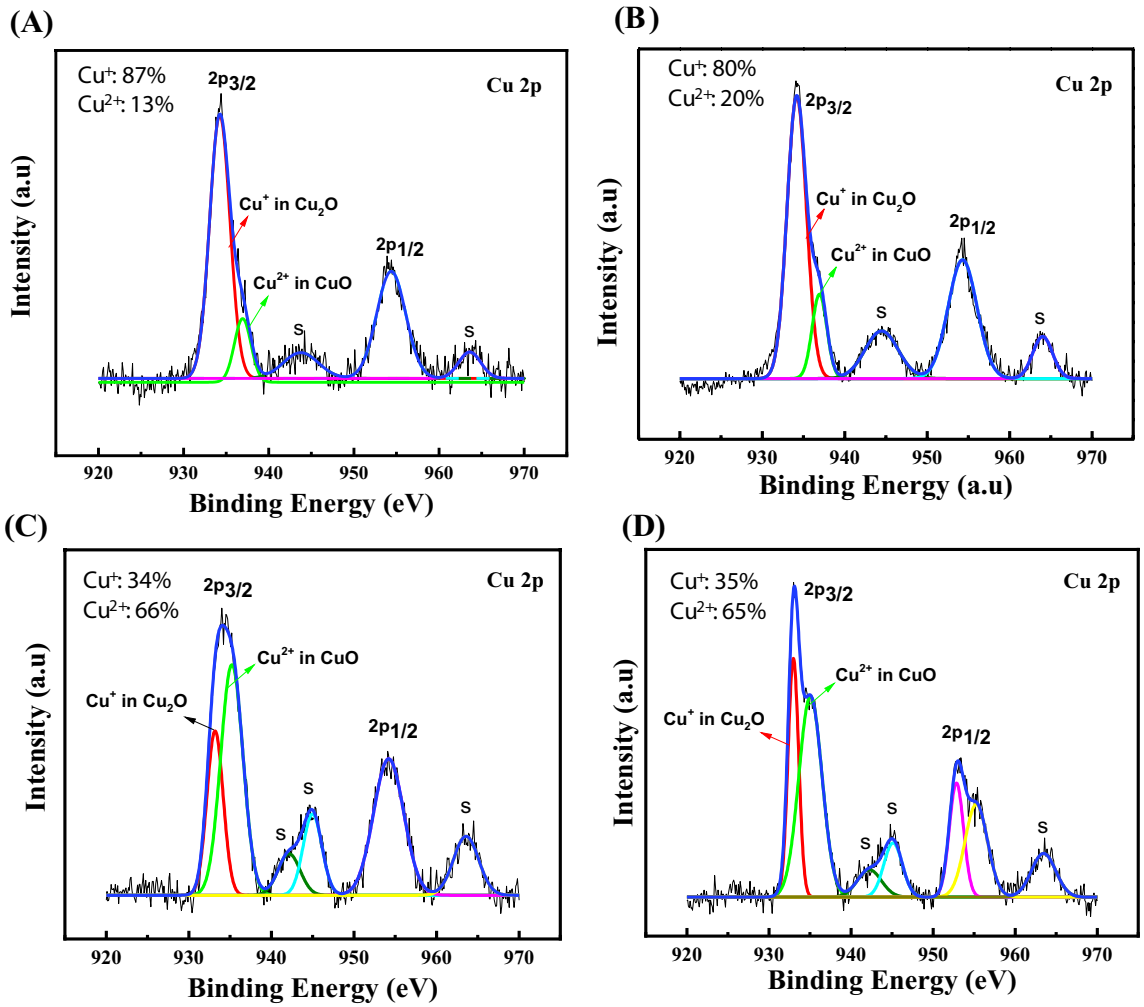


**Fig. 2** Deconvoluted Cu 2p core level region X-ray photoelectron spectra of **a** $Cu_2O$/Cuo, **b** $Cu_2O$/CuO_Cl, **c** $Cu_2O$/CuO_Br and **d** $Cu_2O$/CuO_I nanocubes ('s' stands for satellite peak)

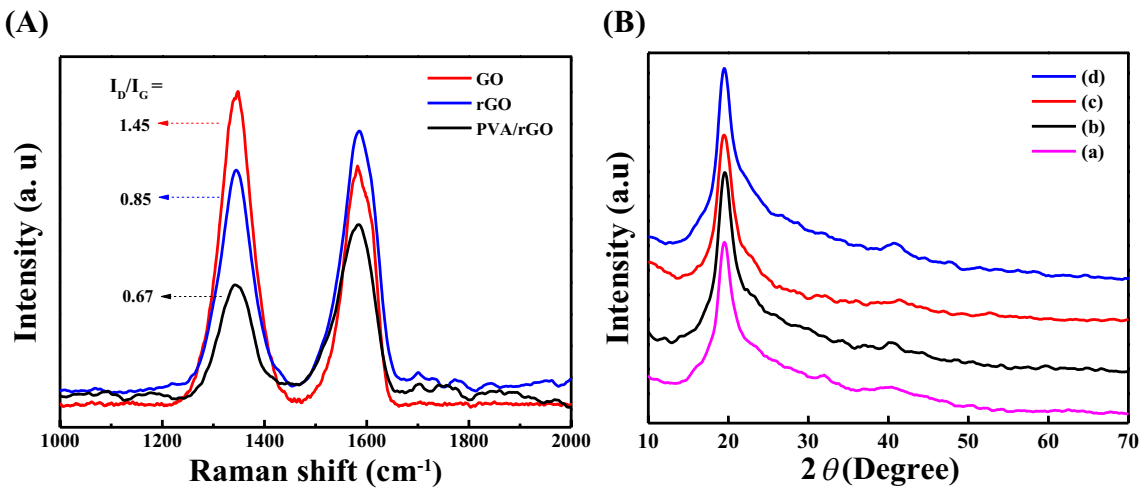


**Fig. 3** (**A**) Raman spectra of GO, rGO and PVA/rGO films, and (**B**) XRD pattern of (a) PVA/rGO/($Cu_2O$/CuO), (b) PVA/rGO/($Cu_2O$/CuO_Cl), (c) PVA/rGO/($Cu_2O$/CuO_Br) and (d) PVA/rGO/($Cu_2O$/CuO_I) films, respectively.

**Table 1** The Zeta potential values of PVA-rGO, $Cu_2O$/CuO and $Cu_2O$/CuO_X (where X = Cl, Br, I) nanocubes

| Material | ζ-potential in mV (SD*) |
|---|---|
| PVA-rGO | − 6.34 (± 0.14) |
| $Cu_2O$/CuO | − 19.16 (± 0.29) |
| $Cu_2O$/CuO_Cl | − 13.50 (± 0.06) |
| $Cu_2O$/CuO_Br | − 38.43 (± 0.15) |
| $Cu_2O$/CuO_I | − 36.26 (± 0.39) |

*Standard deviation calculated from four successive measurements

relatively stronger columbic interaction of $Cu_2O$/CuO_Cl nanocubes with the PVA/rGO matrix could lead to the least charge transfer resistance, hence the higher $CO_2$RR activity. To accomplish the optimum $CO_2$RR activity, the thickness of the films and loading of $Cu_2O$/CuO_Cl were studied by varying the volumes of PVA/rGO/($Cu_2O$/CuO_Cl) and $Cu_2O$/CuO_Cl solutions, respectively.

The preparation of the thin films on microscopic slides is schematically represented in Scheme S1. PVA/rGO/($Cu_2O$/CuO) solution was sonicated for 1 h to form an ink-like dispersion. The resulting ink (1 mL) was dropped on to (5 × 2) $cm^2$ area of a microscopic glass slide and dried overnight at room temperature to form PVA/rGO/($Cu_2O$/CuO) film. Similarly, PVA/rGO/($Cu_2O$/CuO_Cl), PVA/rGO/($Cu_2O$/CuO_Br), and PVA/rGO/($Cu_2O$/CuO_I), thin films were prepared using ~ 1.31 µg of $Cu_2O$/CuO_Cl, $Cu_2O$/CuO_Br, and $Cu_2O$/CuO_I solutions, respectively. In Fig. 3b, XRD patterns of all the films displayed a broad peak at 2θ value of 19.5° which corresponds to PVA [39]. The characteristic peaks of $Cu_2O$/CuO or $Cu_2O$/CuO_X did not appear because of their ultra-low (0.87–3.06 µg/$cm^2$) loadings and their existence within the PVA/rGO sheets. The mechanical properties of PVA fibers facilitate the formation of a stable and flexible film. The free-standing PVA/rGO/($Cu_2O$/CuO_Cl) thin film is stable after twisting, and tape tests, showing its mechanical strength which is one of the desired properties of free-standing working electrodes (Figure S2). In the case of free-standing electrodes, no direct support of the current collector is used; hence the intrinsic electrical conductivity of thin films itself needs to be high enough to conduct the electrons. Electrical conductivity of PVA/rGO/($Cu_2O$/CuO), PVA/rGO/($Cu_2O$/CuO_Cl), PVA/rGO/($Cu_2O$/CuO_Br), and PVA/rGO/($Cu_2O$/CuO_I), films were measured to be 0.160, 0.182, 0.185 and 0.380 S/m via two probe-method, respectively. These conductivity values are four orders of magnitude lower than that of the reported rGO (2420 S/m) and 30 times lower than the rGO/PVA [39, 40]. The presence of non-conducting PVA on to the rGO sheets could decrease the conductivity of the free-standing thin films.

## 3.2 Electrochemical reduction of $CO_2$

Figure 4a shows the CVs of PVA/rGO/($Cu_2O$/CuO_Cl) film recorded in the $N_2$-saturated and $CO_2$-saturated 0.5 M $KHCO_3$ solution. The enhanced current density exhibited in $CO_2$-saturated 0.5 M $KHCO_3$ electrolyte indicates the electrocatalytic ability of PVA/rGO/($Cu_2O$/CuO_Cl) thin film for $CO_2$RR. Figure 4b shows CVs of free-standing films of PVA/rGO/($Cu_2O$/CuO), PVA/rGO/($Cu_2O$/CuO_Cl), PVA/rGO/($Cu_2O$/CuO_Br), and PVA/rGO/($Cu_2O$/CuO_I), prepared from different sized $Cu_2O$/CuO_X nanocubes, recorded at a scan rate of 20 mV $s^{-1}$ in $CO_2$-saturated 0.5 M $KHCO_3$ solution at 25 °C. The PVA/rGO/($Cu_2O$/CuO_Cl) thin film displayed a remarkable $CO_2$RR activity, in terms of low onset potential and higher current densities in comparison to that of PVA/rGO/($Cu_2O$/CuO), PVA/rGO/($Cu_2O$/CuO_Br), and PVA/rGO/($Cu_2O$/CuO_I) thin films. PVA/rGO/($Cu_2O$/CuO_Cl) film showed an onset potential of − 0.40 V vs. RHE for $CO_2$RR, which is much lower than that of PVA/rGO/($Cu_2O$/CuO), (− 0.43 V vs. RHE), PVA/rGO/($Cu_2O$/CuO_Br) (− 0.80 V vs. RHE) and PVA/rGO/($Cu_2O$/CuO_I), (− 0.66 V vs. RHE) films. It exhibited a current density of 0.12 mA $cm^{-2}$ at − 0.80 V vs. RHE, which is ~ 7 times higher than that of the other films studied for $CO_2$RR (see Figure S3). The superior $CO_2$RR activity of PVA/rGO/($Cu_2O$/CuO_Cl) thin film is likely due to a large number of active sites and relatively smaller sizes of $Cu_2O$ nanocubes. $Cl^-$ ions could suppress the unwanted hydrogen product, which increases the $CO_2$RR activity and selectivity of PVA/rGO/($Cu_2O$/CuO_Cl) thin film [32, 41].

Further, $CO_2$RR activity of PVA/rGO/($Cu_2O$/CuO_Cl) thin film was optimized with respect to $Cu_2O$/CuO loadings ($\mu g_{Cu_2O}$/CuO_Cl/$mg_{rGO}$). By using aliquots of 100–350 µL) of $Cu_2O$/CuO_Cl solutions, various amounts (0.87–3.06 µg) of $Cu_2O$/CuO_Cl were loaded onto each one mg of PVA/rGO composite. Figure S4(B) shows the $CO_2$RR activity of PVA/rGO/($Cu_2O$/CuO_Cl) film at various loadings of $Cu_2O$/CuO-Cl nanocubes. Upon increasing the $Cu_2O$/CuO_Cl loadings from 0.87 to 2.19 µg, an increase in current density and a decrease in the onset potential were noted. Further increase in $Cu_2O$ loading to 3.12 µg resulted in poor $CO_2$RR activity, revealing that higher $Cu_2O$ loadings could lead to aggregation of particles that cause the lower number of active sites for $CO_2$RR. Thus, optimum $CO_2$RR activity was found at a $Cu_2O$/CuO_Cl loading of 1.31 µg. We then optimized the film thickness by changing the rGO loading per unit area to further enhance $CO_2$RR activity. Figure S4(A) shows the $CO_2$RR activity of films prepared at different loadings of rGO. High rGO loadings could decrease the surface area, deform the regular arrangements of PVA chains of PVA/rGO/($Cu_2O$/CuO_Cl) films which led to the poor $CO_2$RR activity [42]. The thin film prepared using 0.492 mg of rGO showed the optimum

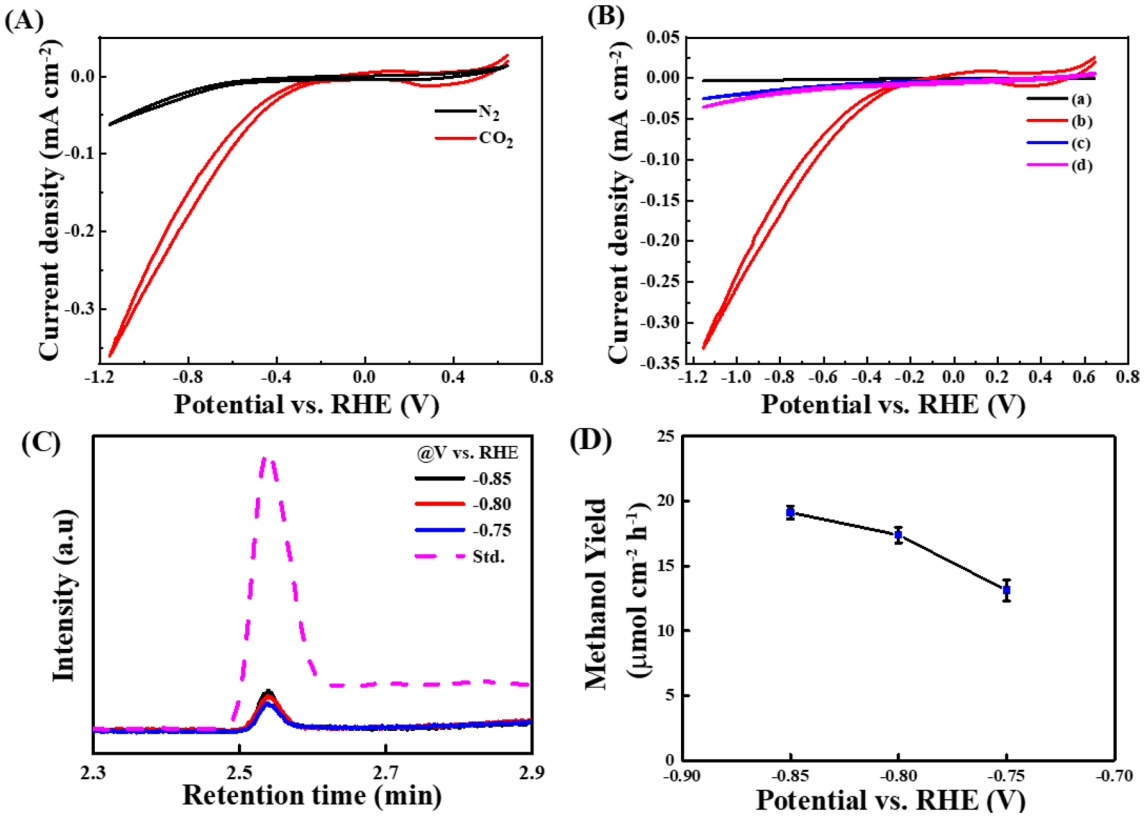


**Fig. 4** Comparison of cyclic voltammograms of **A** PVA/rGO/($Cu_2O$/CuO_Cl) film in $N_2$–, CO2-saturated 0.5 M $KHCO_3$, **B** (a) PVA/rGO/($Cu_2O$/CuO), (b) PVA/rGO/($Cu_2O$/CuO_Cl), (c) PVA/rGO/($Cu_2O$/CuO_Br) and (d) PVA/rGO/($Cu_2O$/CuO_I) films in $CO_2$-saturated 0.5 M $KHCO_3$ (pH 7.6) at the scan rate of 20 mV $s^{-1}$, 25 °C; **C** comparison of gas chromatograms of standard (std.) solution (250 μM methanol in 0.5 M $KHCO_3$) and 0.5 M $KHCO_3$ electrolyte collected after 1 h of $CO_2$RR on PVA/rGO/($Cu_2O$/CuO_Cl) film at (a) − 0.85, (b) − 0.80 and (c) − 0.75 V vs. RHE; **D** methanol formation rates (μmol $cm^{-2}$ $h^{-1}$) determined at different potentials for the film (a).

$CO_2$RR activity. Figure S5 shows the cross-sectional SEM images of the respective films prepared with different rGO loadings. The thickness of the films prepared using the rGO loadings of 0.246, 0.492, 0.738 and 0.984 mg were 11, 14, 16, and 32 μm, respectively.

### 3.3 Analysis of products

Chronoamperometry was used to monitor the product of electrolysis of $CO_2$ in the potential range between − 0.75 to − 0.85 V vs. RHE for 1 h. In order to identify and quantify the products during the course of $CO_2$RR, controlled potential electrolysis was carried out at potentials of − 0.75, − 0.80 and − 0.85 V vs. RHE for 1 h in 0.5 M $KHCO_3$ solution. GC–MS was used to analyze the liquid products formed during the $CO_2$RR. Figure 4c shows the GC spectra of standard methanol solution and that of the solutions subjected to electrolysis of $CO_2$ at different potentials using the free-standing PVA/rGO/($Cu_2O$/CuO_Cl) thin film. A sharp peak corresponding to methanol was observed at a retention time of 2.54 min. We observed only methanol as a product in the liquid phase, which confirms the high selectivity of the PVA/rGO/($Cu_2O$/CuO_Cl) thin film towards methanol formation in $CO_2$RR. The amount of methanol formed was then determined using a calibration curve of the peak area against the concentration of standard methanol solution in 0.5 M $KHCO_3$ (Figure S6). The amounts of methanol formed at the potentials of − 0.75, − 0.80 and − 0.85 V vs. RHE for 1 h were found to be 27, 35 and 39 μmol, respectively (Fig. 4d). The highest methanol yield of 19.5 μmol $cm^{-2}$ $h^{-1}$ was observed at − 0.85 V vs. RHE. Le et al. have reported the methanol yield of 43 μmol $cm^{-2}$ $h^{-1}$ at − 1.32 V vs. RHE for electrodeposited $Cu_2O$ in 0.5 M $KHCO_3$, however, the onset potential for the $CO_2$RR was observed at high overpotentials (− 0.75 V vs. RHE) [43]. Methanol yield and onset potential of PVA/rGO/($Cu_2O$/CuO_Cl) film for $CO_2$RR are superior to that of the several catalysts reported in the literature (Table 2) [44–48]. The $CO_2$RR experiment was conducted using chronoamperometric technique (− 0.75, − 0.80 and − 0.85 V vs. RHE) in a sealed 2 mL reaction vessel to quantify the gas and liquid products in $CO_2$ saturated 0.5 M $KHCO_3$. Figure S7 displays the i–t curves for $CO_2$RR on PVA/rGO/($Cu_2O$/CuO_Cl) in 0.5 M $KHCO_3$ at − 0.75, − 0.80 and − 0.85 V vs. RHE. Figure S8 represents

**Table 2** Comparison of onset potentials and methanol yields of various electrocatalysts for $CO_2RR$ reported in the literature

| S. no. | Catalyst | Electrolyte | Onset for $CO_2RR$, (V vs. RHE) | Methanol yields ($\mu mol\ cm^{-2}\ h^{-1}$), V vs. RHE | Ref. |
|---|---|---|---|---|---|
| 1 | PVA/rGO/($Cu_2O$ /CuO_Cl) film | 0.5 M $KHCO_3$ | − 0.40 | 19.5, − 0.80 | This work |
| 2 | $Cu_2O$/polypyrrole | 0.5 M $KHCO_3$ | − 0.43 | $1\times10^{-2}$, − 0.85 | [23] |
| 3 | Electrodeposited $Cu_2O$ | 0.5 M $KHCO_3$ | − 0.75 | 43, − 1.32 | [43] |
| 4 | Anodized Cu | 0.5 M $KHCO_3$ | − 0.16 | 0.01, − 1.66 | [34] |
| 5 | $Cu_{88}Sn_6Pb_6$ alloy | 0.5 M NaCl + 1.5 M HCl | − 0.58 | 0.3, − 1.0 | [51] |
| 6 | Cu nanocluster/(1010) ZnO | 0.1 M $K_2HPO_4$ +0.1 M KH2PO4 | − 0.55 | $1.53\times10^{-3}$, − 1.2 | [52] |
| 7 | $[Cu_3(\mu6\text{-}C_9H_3O_6)_2\ (OH_2)_3]_n$ | 0.5 M $KHCO_3$ | − 0.8 | 0.06, − 0.70 | [53] |
| 8 | $Cu_2O$/ZnO | 0.5 M $KHCO_3$ + 10 mM of 2 methyl pyridine | − 0.7 | 0.02, − 0.80 | [54] |
| 9 | $Cu_2O$/ZnO (1:1) | 0.5 M $KHCO_3$ | − 1.0 | 0.02, − 1.1 | [55] |

the calibration plot for $H_2$ gas. The GC calibration line for $H_2$ gas was obtained by injecting the known volumes of $H_2$ from 2 to 25 µL corresponding to 0.1 to 1.2 umol of $H_2$ gas, respectively. A 500 µL of gas was collected from the 2 mL headspace reaction vessel after 1 h of $CO_2RR$ using gas-tight syringe followed by sample injection to GC instrument. Figure S9 shows the GC plot obtained at (A) − 0.75, (B) − 0.80, and (C) − 0.85 V vs. RHE. The amount of $H_2$ gas was calculated to be $1.60\times10^{-6}$, $0.92\times10^{-6}$ and $2\times10^{-6}$ µmol $cm^{-2}$ at − 0.75, − 0.80 and − 0.85 V vs. RHE, respectively. The FE for the $H_2$ was calculated to be 20, 14 and 32% at − 0.75, − 0.80 and − 0.85 V vs. RHE, respectively. The amount of methanol was quantified using $^1$H-NMR at − 0.75, − 0.80 and − 0.85 V vs. RHE. A 35 µL of standard solution and 500 µL of 0.5 M $KHCO_3$ was mixed thoroughly and analyzed with AVIII600 NMR. Figure 5 shows the $^1$H-NMR of the electrolyte which was collected after 1 h of $CO_2RR$ at different potentials. The $^1$H-NMR peaks around 4.59, 3.17 and 2.5 ppm indicate the $H_2O$, methanol and DMSO, respectively. The Polyvinyl alcohol, which is employed in the thin film electrodes preparation, was dissolved in to the electrolyte. The 'methene' (2) and 'methine'(1) protons were appeared at 3.42 and 0.9 ppm, respectively [49]. The FE for the methanol was found to be 63, 43 and 59% at − 0.75, − 0.80 and − 0.85 V vs. RHE, respectively. Table S1 lists the amount and FE for methanol and $H_2$ gas. The FE % is higher than several reported catalysts for methanol production in $CO_2RR$ [21, 46, 48, 50]. Figure 6 displays the FE % for the methanol and $H_2$ gas in $CO_2RR$ on PVA/rGO/($Cu_2O$/CuO_Cl). The durability in methanol production of

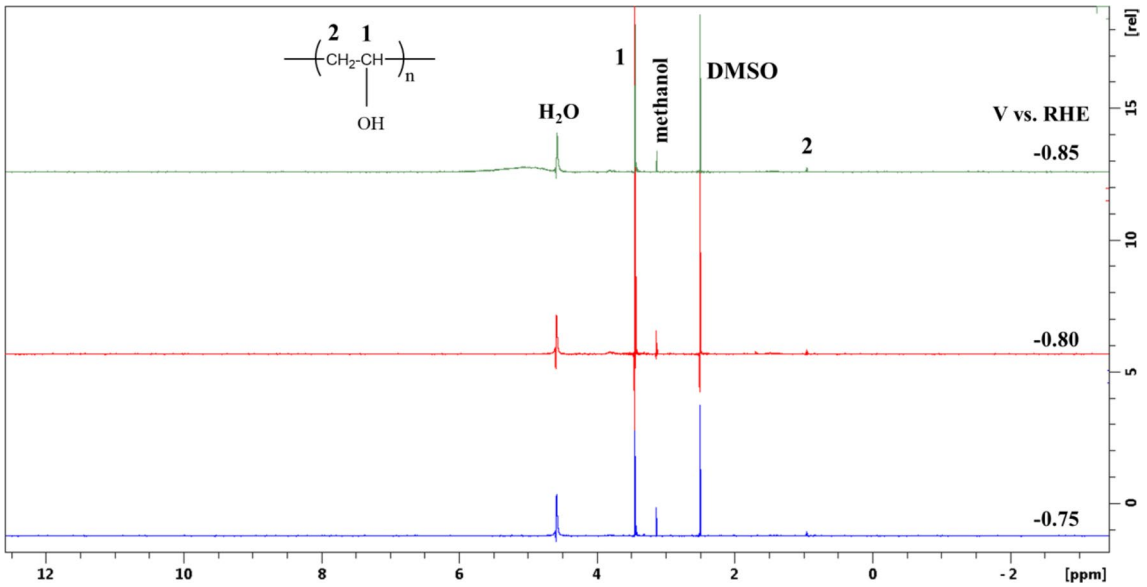


**Fig. 5** $^1$H-NMR of the liquid products in CO2RR on PVA/rGO/($Cu_2O$/CuO_Cl) (10 mM DMSO added as an internal standard in $D_2O$ solvent)

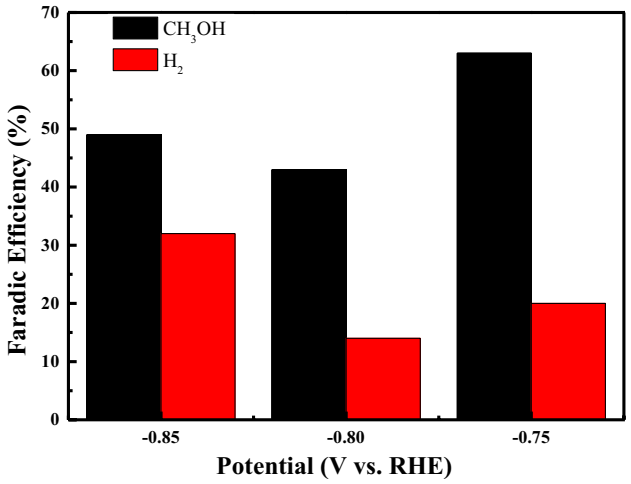


**Fig. 6** Faradaic efficiency for methanol and $H_2$ gas in $CO_2RR$ on PVA/rGO/($Cu_2O$/CuO_Cl) thin film electrode in 0.5 M $KHCO_3$ at − 0.75, − 0.80 and − 0.85 V vs. RHE about 1 h

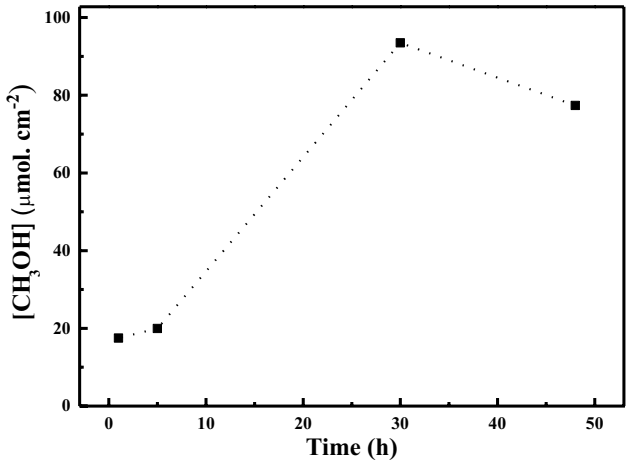


**Fig. 7** The methanol production rates at 1, 5, 30 and 48 h of $CO_2RR$ on PVA/rGO/($Cu_2O$/CuO_Cl) thin film electrode in 0.5 M $KHCO_3$ electrolyte at − 0.75 vs. RHE

PVA/rGO/($Cu_2O$/CuO_Cl) in 0.5 M $KHCO_3$ was evaluated for 48 h. 1 mL of 0.5 M $KHCO_3$ was collected from 25 mL of electrolyte for sampling at respective times followed by introducing 1 mL of $CO_2$ saturated 0.5 M $KHCO_3$. Figure S10 (A) shows the chronoamperometric graph for 48 h and (B) $^1$H-NMR data shows the methanol as a liquid product. The amount of methanol was found to be 18, 20, 93 and 77 μmol $cm^{-2}$ for 1, 5, 30 and 48 h duration, on PVA/rGO/($Cu_2O$/CuO_Cl) at − 0.75 V vs. RHE, respectively (Fig. 7).

Cross-linked PVA with rGO could facilitate the permeability of $CO_2$ molecules through film [51, 52]. PVA molecules show excellent mechanical strength to the film and also acts as supporting units for rGO [53–56]. Partially oxidized $Cu_2O$ nanocubes provide the active sites for $CO_2$ reduction, whereas PVA/rGO matrix enhances the electron transport in the film. Recently, Periasamy et al. have reported that methanol is formed on the $Cu_2O$ surface through the electrochemical reduction of $CO_{2,ads}$ to CO, followed by the hydrogenation of CO to $CH_3O^-$, which reduced further to form methanol [23]. Similar reaction pathways and mechanisms are likely to occur on the surfaces of $Cu_2O$ nanocubes anchored on the surfaces of PVA/rGO leading to the formation of methanol. Although Strasser et al. have doubled the CO production efficiency of Cu electrodes through the direct addition of halides each at a concentration of 0.3 M into the testing electrolyte, their electrochemical behavior under dynamic and stationary potential conditions was different and thus they were unable to generate a valuable hydrocarbon product (methanol) [25]. Unlike this approach, we directly added relatively fewer amounts of halides (10 mM vs. 0.3 M) into the $Cu_2O$ preparation solution and tuned the size of $Cu_2O$ particles by controlling the specific adsorption capacity of halide ions. As a result, we were able to control the surface structures, the active sites, the reaction intermediates, and the rate of methanol formation. The $Cl^-$ ions adsorbed on the surfaces of $Cu_2O$ remarkably accelerates the $CO_2^-$ formation and enhances the CO production. The negative charge induced by the $Cl^-$ ions result in a positive effect leading to a facile protonation/hydrogenation of CO to form $CH_3O^-$ and thus the methanol [25]. The enhanced electron flow from the $Cl^-$ orbital to the vacant $CO_2$ orbital through a nucleophilic attack on the carbon atom of $CO_2$, further enhances the current density, methanol selectivity, and methanol formation rate [57].

## 4 Conclusions

Direct evaporation assisted self-assembly strategy for the fabrication of free-standing thin films was employed using PVA, rGO and partial surface oxidized $Cu_2O$ nanocubes ($Cu_2O$/CuO) on an inexpensive microscopic glass slide. $Cu_2O$/CuO nanocubes were synthesized in the presence of sodium halides (1 mL of 10 mM NaCl, NaBr and NaI) at room temperature. $Cl^-$ ion adsorption over the surface of $Cu_2O$ hindered the adsorption of adatoms to $Cu_2O$ crystal facets and formed 27 ± 2 nm size particles, whereas $Br^-$ and $I^-$ ions did not show notable adsorption on $Cu_2O$ surface and yielded the particles with larger sizes, 62 ± 4 and 207 ± 3 nm, respectively. The high-resolution photoelectron spectrum revealed a small CuO surface phase present over the $Cu_2O$ nanocubes. The ratio of $Cu_2O$: CuO for (a) $Cu_2O$/CuO, (b) $Cu_2O$/CuO_Cl, (c) $Cu_2O$/CuO_Br and (d) $Cu_2O$/CuO_I was calculated to be 87:13, 80:20, 34:66 and 35:65. PVA/rGO/($Cu_2O$/CuO_Cl) film exhibited superior $CO_2$ reduction activity in terms of onset potential (− 0.40 V vs. RHE) and current density (0.12 mA $cm^{-2}$

at − 0.80 V vs. RHE) than that of the PVA/rGO/($Cu_2O$/CuO), PVA/rGO/($Cu_2O$/CuO_Br), and PVA/rGO/($Cu_2O$/CuO_I) thin films. GC–MS analysis revealed the formation of methanol as a single liquid product. Methanol yield of 19.5 µmol $cm^{-2}$ $h^{-1}$ at − 0.85 V vs. RHE is observed on the PVA/rGO/($Cu_2O$/CuO_Cl) thin film. The FE for methanol and $H_2$ gas were found to be 63 and 20% at − 0.75 V vs RHE, respectively, which is the highest FE among the − 0.75, − 0.80 and − 0.85 V vs. RHE. With the advantages of low-cost, flexibility, high mechanical strength, catalytic activity, and stability, the free-standing thin films prepared through direct evaporation assisted self-assembly method holds great potential for the use in electrocatalysis and chemical industries to generate pure methanol.

**Acknowledgements** RS and AS thanks to the MOST (Ministry Of Science and Technology), Taiwan for financial support under project number MOST-108-2112-M-001-049-MY2. We also thank Ms. S.-J. Ji and C.-Y. Chien of the Precious Instrument Center (National Taiwan University, Taiwan) for their assistance in SEM. The assistance of Ms. S.-J. Ji and C.-Y. Chien from the Instrument Center at NTU for TEM measurement is appreciated.

## References

1. Anderson TR, Hawkins E et al (2016) $CO_2$, the greenhouse effect and global warming: from the pioneering work of Arrhenius and Callendar to today's Earth System Models. Endeavour 40(3):178–187
2. Saeidi S, Amin NAS et al (2014) Hydrogenation of $CO_2$ to value-added products—a review and potential future developments. J CO2 Util 5:66–81
3. Albo J, Alvarez-Guerra M et al (2015) Towards the electrochemical conversion of carbon dioxide into methanol. Green Chem 17(4):2304–2324
4. Joghee P, Malik JN et al (2015) A review on direct methanol fuel cells—in the perspective of energy and sustainability. MRS Energy Sustain 2:E3
5. Ganesh I (2014) Conversion of carbon dioxide into methanol—a potential liquid fuel: Fundamental challenges and opportunities (a review). Renew Sustain Energy Rev 31:221–257
6. Luu MT, Milani D et al (2015) A comparative study of $CO_2$ utilization in methanol synthesis with various syngas production technologies. J CO2 Util 12:62–76
7. von der Assen N, Voll P et al (2014) Life cycle assessment of $CO_2$ capture and utilization: a tutorial review. Chem Soc Rev 43(23):7982–7994
8. Gao D, Cai F, Wang G et al (2017) Nanostructured heterogeneous catalysts for electrochemical reduction of $CO_2$. Curr Opin Green Sustain Chem 3:39–44
9. Lim RJ, Xie M, Sk MA et al (2014) A review on the electrochemical reduction of $CO_2$ in fuel cells, metal electrodes and molecular catalysts. Catal Today 233:169–180
10. Qiao J, Liu Y, Hong F et al (2014) A review of catalysts for the electroreduction of carbon dioxide to produce low-carbon fuels. Chem Soc Rev 43(2):631–675
11. Kumar B, Brian JP et al (2016) New trends in the development of heterogeneous catalysts for electrochemical $CO_2$ reduction. Catal Today 270:19–30
12. Hori Y, Wakebe H et al (1994) Electrocatalytic process of CO selectivity in electrochemical reduction of $CO_2$ at metal electrodes in aqueous media. Electrochim Acta 39(11):1833–1839
13. Raciti D, Wang C (2018) Recent advances in $CO_2$ reduction Electrocatalysis on copper. ACS Energy Lett 3(7):1545–1556
14. Schreier M, Luo J et al (2016) Covalent immobilization of a molecular catalyst on $Cu_2O$ photocathodes for $CO_2$ reduction. J Am Chem Soc 138(6):1938–1946
15. Peterson AA, Abild-Pedersen F et al (2010) How copper catalyzes the electroreduction of carbon dioxide into hydrocarbon fuels. Energy Environ Sci 3(9):1311–1315
16. Nitopi S, Bertheussen E et al (2019) Progress and perspectives of electrochemical $CO_2$ reduction on copper in aqueous electrolyte. Chem Rev 119(12):7610–7672
17. Raciti D, Wang Y et al (2018) Three-dimensional hierarchical copper-based nanostructures as advanced electrocatalysts for $CO_2$ reduction. ACS Appl Energy Mater 1(6):2392–2398
18. Gu Z, Shen H et al (2018) Nanostructured copper-based electrocatalysts for $CO_2$ reduction. Small Methods 2(11):1800121
19. Irfan Malik M, Malaibari ZO et al (2016) Electrochemical reduction of $CO_2$ to methanol over MWCNTs impregnated with $Cu_2O$. Chem Eng Sci 152:468–477
20. An X, Li K et al (2014) $Cu_2O$/reduced graphene oxide composites for the photocatalytic conversion of $CO_2$. Chemsuschem 7(4):1086–1093
21. Albo J, Irabien A (2016) $Cu_2O$-loaded gas diffusion electrodes for the continuous electrochemical reduction of $CO_2$ to methanol. J Catal 343:232–239
22. Chang T-Y, Liang R-M et al (2009) Electrochemical reduction of $CO_2$ by $Cu_2O$-catalyzed carbon clothes. Mater Lett 63(12):1001–1003
23. Periasamy AP, Ravindranath R et al (2018) Facet- and structure-dependent catalytic activity of cuprous oxide/polypyrrole particles towards the efficient reduction of carbon dioxide to methanol. Nanoscale 10(25):11869–11880
24. Salazar-Villalpando MD (2011) Effect of electrolyte on the electrochemical reduction of $CO_2$. ECS Trans 33(27):77–88
25. Varela AS, Ju W et al (2016) Tuning the catalytic activity and selectivity of Cu for $CO_2$ electroreduction in the presence of halides. ACS Catal 6(4):2136–2144
26. Feng H, Li Y et al (2012) Strong reduced graphene oxide–polymer composites: hydrogels and wires. RSC Adv 2(17):6988–6993
27. Sahoo NG, Pan Y et al (2012) Graphene-based materials for energy conversion. Adv Mater 24(30):4203–4210
28. Yang Z, Chiang CK et al (2007) Synthesis of fluorescent and photovoltaic $Cu_2O$ nanocubes. Nanotechnology 19(2):025604
29. Tang Z, Kwon H et al (2017) Role of halide ions for controlling morphology of copper nanocrystals in aqueous solution. ChemistrySelect 2(17):4655–4661
30. Meena SK, Celiksoy S et al (2016) The role of halide ions in the anisotropic growth of gold nanoparticles: a microscopic, atomistic perspective. Phys Chem Chem Phys 18(19):13246–13254
31. Rai A, Singh A et al (2006) Role of halide ions and temperature on the morphology of biologically synthesized gold nanotriangles. Langmuir 22(2):736–741
32. Hsieh Y-C, Senanayake SD et al (2015) Effect of chloride anions on the synthesis and enhanced catalytic activity of silver nanocoral electrodes for $CO_2$ electroreduction. ACS Catal 5(9):5349–5356
33. Ignaczak A, Gomes JANF (1997) Quantum calculations on the adsorption of halide ions on the noble metals. J Electroanal Chem 420(1):71–78
34. Frese KW (1991) Electrochemical reduction of $CO_2$ at intentionally oxidized copper electrodes. J Electrochem Soc 138(11):3338–3344

35. Wang M, Ren X et al (2020) Selective electroreduction of $CO_2$ to CO over co-electrodeposited dendritic core-shell indium-doped Cu@Cu2O catalyst. J CO Util 37:204–212
36. Gerson AR, Jasieniak M (2008) In: Duo WD, Yao SC, Liang WF, Cheng ZL, Long H (eds) Proceedings of the XXIV international minerals processing congress. Science Press, Beijing, pp 1054–1063
37. Tripathi S, Mehrotra GK et al (2009) Physicochemical and bioactivity of cross-linked chitosan–PVA film for food packaging applications. Int J Biol Macromol 45(4):372–376
38. Park S, Hu Y et al (2012) Chemical structures of hydrazine-treated graphene oxide and generation of aromatic nitrogen doping. Nat Commun 3(1):638
39. Yang J-H, Lee Y-D (2012) Highly electrically conductive rGO/PVA composites with a network dispersive nanostructure. J Mater Chem 22(17):8512–8517
40. Stankovich S, Dikin DA et al (2007) Synthesis of graphene-based nanosheets via chemical reduction of exfoliated graphite oxide. Carbon 45(7):1558–1565
41. Quan F, Zhong D et al (2015) A highly efficient zinc catalyst for selective electroreduction of carbon dioxide in aqueous NaCl solution. J Mater Chem A 3(32):16409–16413
42. Zhao X, Zhang Q et al (2010) Enhanced mechanical properties of graphene-based poly(vinyl alcohol) composites. Macromolecules 43(5):2357–2363
43. Le M, Ren M et al (2011) Electrochemical reduction of $CO_2$ to $CH_3OH$ at copper oxide surfaces. J Electrochem Soc 158(5):E45–E49
44. Schizodimou A, Kyriacou G (2012) Acceleration of the reduction of carbon dioxide in the presence of multivalent cations. Electrochim Acta 78:171–176
45. Jia F, Yu X et al (2014) Enhanced selectivity for the electrochemical reduction of $CO_2$ to alcohols in aqueous solution with nanostructured Cu–Au alloy as catalyst. J Power Sources 252:85–89
46. Albo J, Vallejo D et al (2017) Copper-based metal-organic porous materials for $CO_2$ electrocatalytic reduction to alcohols. Chemsuschem 10(6):1100–1109
47. Albo J, Beobide G et al (2017) Methanol electrosynthesis from $CO_2$ at $Cu_2O$/ZnO prompted by pyridine-based aqueous solutions. J CO2 Util 18:164–172
48. Albo J, Sáez A et al (2015) Production of methanol from $CO_2$ electroreduction at $Cu_2O$ and $Cu_2O$/ZnO-based electrodes in aqueous solution. Appl Catal 176–177:709–717
49. Li B, Gao Y, Guo L, Fan Y, Kawazoe N, Fan H, Zhang X, Chen G (2018) Synthesis of photo-reactive poly (vinyl alcohol) and construction of scaffold-free cartilage like pellets in vitro. Regen Biomater 5(3):159–166
50. Yuan J, Wang X, Gu C, Sun J, Ding W, Wei J, Zuo X, Hao C (2017) Photoelectrocatalytic reduction of carbon dioxide to methanol at cuprous oxide foam cathode. RSC Adv 7(40):24933–24939
51. Liu Y, Su Y et al (2018) Asymmetric aerogel membranes with ultrafast water permeation for the separation of oil-in-water emulsion. ACS Appl Mater Interfaces 10(31):26546–26554
52. Mondal A, Mandal B (2014) Novel $CO_2$-selective cross-linked poly(vinyl alcohol)/polyvinylpyrrolidone blend membrane containing amine carrier for $CO_2$–$N_2$ separation: synthesis, characterization, and gas permeation study. Ind Eng Chem Res 53(51):19736–19746
53. Wang T, Li Y et al (2015) Preparation of flexible reduced graphene oxide/poly(vinyl alcohol) film with superior microwave absorption properties. RSC Adv 5(108):88958–88964
54. Zhang X, Zhou Y et al (2017) In-situ reduced graphene oxide-polyvinyl alcohol composite coatings as protective layers on magnesium substrates. Prog Nat Sci Mater Int 27(3):326–328
55. Kim S, Shimazu J et al (2017) Thermal conductivity of graphene oxide-enhanced polyvinyl alcohol composites depending on molecular interaction. Polymer 129:201–206
56. Xu Y, Hong W et al (2009) Strong and ductile poly(vinyl alcohol)/graphene oxide composite films with a layered structure. Carbon 47(15):3538–3543
57. Ogura K, Salazar-Villalpando MD (2011) $CO_2$ electrochemical reduction via adsorbed halide anions. JOM 63(1):35–38



## Affiliations

**Anjaiah Sheelam[1] · Adil Muneeb[1,2] · Biva Talukdar[3] · Rini Ravindranath[4] · Song-Jeng Huang[2] · Chun-Hong Kuo[3] · Raman Sankar[1]**

✉ Raman Sankar
sankarndf@gmail.com; sankarraman@gate.sinica.edu.tw

[1] Institute of Physics, Academia Sinica, Taipei 11529, Taiwan

[2] Mechanical Engineering, National Taiwan University of Science and Technology, Taipei 10607, Taiwan

[3] Institute of Chemistry, Academia Sinica, Taipei 11529, Taiwan

[4] Department of Chemistry, National Taiwan University, Taipei 10617, Taiwan